IMPLEMENTATION OF THE EXTENDED FINITE ELEMENT METHOD (XFEM) IN THE ABAQUS SOFTWARE PACKAGE

A Thesis
Presented to
The Academic Faculty

By

Michael James McNary

In Partial Fulfillment
Of the Requirements for the Degree
Master of Science in Mechanical Engineering

Georgia Institute of Technology
May 7, 2009

IMPLEMENTATION OF THE EXTENDED FINITE ELEMENT METHOD (XFEM) IN THE ABAQUS SOFTWARE PACKAGE

Approved by:

Professor Mohammed Cherkaoui,
Committee Chair
School of Mechanical Engineering
Georgia Institute of Technology

Professor Richard Neu
School of Mechanical Engineering
Georgia Institute of Technology

Dr. Olaf van der Sluis
Department of Precision and Microsystems Engineering
Delft University, Delft, The Netherlands

Date Approved: May 7, 2009

To my mother,

Arnelle Jean McNary,

who never wavered in her support

during the long, dark night;

and to my Father,

James Joseph McNary,

who taught me to immmmmmprovise

ACKNOWLEDGEMENTS

I want to thank my academic advisor, Dr. Mohammed Cherkaoui, for his work arranging the partnership with Philips and his help through all phases of the research. His belief in the benefits of working with Industry have greatly benefitted all of his students.

I also wish to thank my industry advisor at Philips, Dr. Olaf van der Sluis. His day-to-day mentoring of one who was so new to the whole concept of finite element analysis took great patience.

To Josyane Roschitz, who somehow coordinated the activities of actors in three countries, while at the same time helping me navigate life in a foreign country, I am greatly indebted, as are all the students of GTL.

Finally, I would like to thank the Good Lord, who has blessed me with so much, and given me far more opportunities than I could ever deserve.

TABLE OF CONTENTS

LIST OF TABLES

LIST OF FIGURES

SUMMARY

This work describes the implementation of the eXtended Finite Element Method (XFEM) in the Abaqus software package. A user-defined element was developed containing the analytical functions relating to homogeneous and interface fracture mechanics. The long-term goal of such work is to increase the ability to analyze fractures and other imperfections in multimaterial systems containing large elastic mismatches, such as flexible electronics. A review of XFEM-related literature is presented, as well as an overview of fracture mechanics for both homogeneous and interface systems. The theoretical basis of the XFEM is then covered, including the concepts of Partition of Unity and stress intensity factor evaluation. Finally, numerical results of the implementation are compared to several benchmark cases, along with conclusions and suggestions for future work.

CHAPTER I

INTRODUCTION

Modern multilayered materials must span a wide range of properties, especially so in the area of digital technology. Two such examples are flexible displays and stretchable electronics, both of which promise to bring digital technology into many areas where today there exist only ink, paper, and fabric. One of the major hurdles to their development is the difficulty of accurately modeling their defining characteristic - the region of high elastic mismatch between the relatively stiff electronic components and the flexible substrate. The standard finite element analyses currently used require extremely fine meshes in the region of such interfaces, even more so when discontinuities such as fractures or voids are present. To this high computational cost is added the time needed to construct a suitable mesh conforming to the model's various interface geometries. These are the two main reasons that make the studying of such problems computationally very costly, sometimes prohibitively so.

The eXtended Finite Element Method (XFEM) offers a way to resolve, or, at the very least, to mitigate these issues. In the method, additional nodal degrees of freedom allow the incorporation of *a priori* knowledge of a system's behavior - in the present work, equations governing interface fracture mechanics - to greatly reduce the cost of an analysis.

The XFEM initially grew out of the Partition of Unity Method (covered in Section 3.2) and was originally applied to 2D linearly elastic fracture in isotropic materials with small deformations [3], [26]. It has since been applied to the study of problems in three dimensions [13], an especially troublesome area for the standard FEM due to the considerable difficulty of explicitly modeling the two dimensional crack surface,

which demanded significant mesh refinement along the entire crack front. The XFEM was extended to cover problems containing multiple fractures [6], another class of problems that have considerable costs associated with mesh-creation. Applications involving the large displacements and rotations of finite strains have also been studied [22]. Several types of brittle materials have received attention, including concrete [27], polycrystalline microstructures[35] and polycrystals with discontinuous grain boundaries [32], as have fractures in plastic media [10]. Quasi-static crack initiation and propagation in two [7] and three dimensions [2] has been explored. Several types of dynamic crack growth have also been the focus of researchers [4],[42]. Fatigue fracture has been studied, specifically thermally induced fatigue in integrated circuits [34] and three dimensional fatigue propagation [36].

All of the above work was done with regard to homogeneous fractures. Only recently has much XFEM work been done in the area of interface fracture mechanics, but it is fast becoming an area of intense study. Interface material failure [14], [37], [17], multiscale failure in composites [15], and three dimensional large plasticity deformations at interfaces [20] have all received attention. Computational issues relating to the difference between homogeneous and interface analyses with the XFEM have also been studied [31].

The XFEM has even been applied to areas outside solid mechanics. Taking advantage of the XFEM's ability to easily track a moving boundary, the method has been applied to the study of two-phase fluids [5], rigid particles in Stokes flow [40], and fluid-structure interactions [12], [43], [8]. The growth of biofilms [9], [33] and evolving crack patterns in thin films [23] have also been modeled using the XFEM.

This research is concerned solely with two dimensional quasi-static linear elastic fracture mechanics (LEFM). This may seem a rather limited scope when viewed against the whole discipline of fracture mechanics (three dimensionality, dynamic events, large rotations/deformations, material plasticity, etc.). However, it is both a

necessary first step, as well as one with a surprising number of real world applications - these arising primarily from the judicious simplification of more complex problems. It will be the job of future researchers, as always, to extend the current implementation to some of the aforementioned fields.

For the most part, work in the area of the XFEM has been conducted with programs constructed by the researchers themselves, representing a huge investment in time and effort. With one exception [17], no work has been done within the framework of a commercial finite element package, despite the benefits in time, portability, and the possibility of coupling the XFEM analysis to built-in analysis tools.

This thesis presents such an implementation, in the Abaqus software package, to study interface fracture mechanics. Chapter 2 contains a short review of bulk and interface fracture mechanics theory. The eXtended Finite Element Method is detailed in Chapter 3 along with information on the calculation of stress intensity factors for crack analysis. Chapter 4 covers some issues relating to Abaqus-specific XFEM implementation, and Chapter 5 presents numerical results from several standard benchmark tests, for both homogeneous and interface fracture. Conclusions and suggestions of future work are given in Chapter 6.

CHAPTER II

FRACTURE MECHANICS

2.1 Bulk Fracture Mechanics

Bulk fracture mechanics is concerned with systems where only a single material factors in to the fracture analysis. Even in multimaterial structures, the governing equations hold as long as the fracture affects only one of the materials. The term *crack* will be used to denote any physical discontinuity in the material such as voids or fractures.

When a given crack is subjected to loading, these loads can be decomposed into three modes, as shown in Figure 1. Mode I is analogous to tension normal to the crack, mode II corresponds to in-plane shear, and mode III is out-of–plane shear. Plane strain conditions are assumed for the present work and therefore mode III loading may be neglected. A single type of loading tends to be the exception, rather than the rule, and so the term mode-mixity is used when there is more than one loading mode operating on a given crack [1].

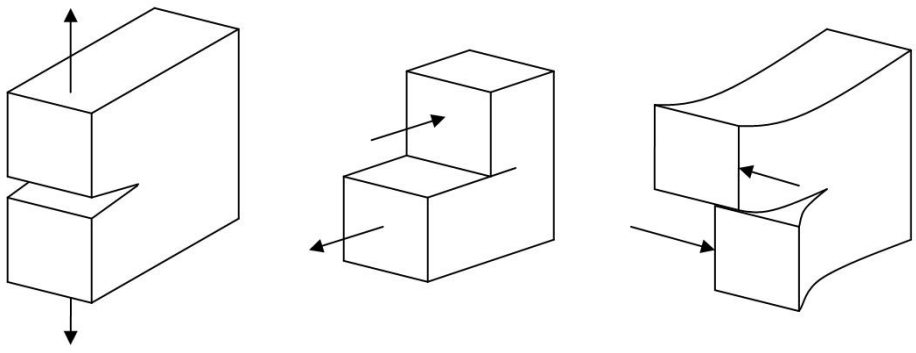

Figure 1: Loading modes I, II, III

One of the central assumptions of fracture mechanics is that, if one get sufficiently close to the crack tip, the stress, strain, and displacement fields become independent of the specimen geometry and the manner in which the sample is loaded. The fields near the crack tip may then be characterized by the three *stress intensity factors* (SIF) - K_I, K_{II}, and K_{III} - corresponding to the three types of loading shown in Figure 1. The SIF are related to the in-plane traction vector at a distance r ahead of the crack tip by

$$(\sigma_{22} + i\tau_{12})_{\theta=0} = \frac{K_I + iK_{II}}{\sqrt{2\pi r}} \tag{1}$$

with r and θ shown in Figure 2. The relative amount of mode II to mode I loading on a specimen is characterized by the mode angle

$$\psi = \tan^{-1}\left(\frac{K_{II}}{K_I}\right) \tag{2}$$

with $\psi = 0°$ for pure mode I loading, and $\psi = 90°$ for pure mode II.

The resulting Cartesian components of the displacements near the crack tip can be expressed as follows

$$\mathbf{u} = (u_x^I) + (u_x^{II}) + (u_y^I) - (u_y^{II}) \tag{3}$$

$$u_x^I = \frac{K_I}{2\mu}\sqrt{\frac{r}{2\pi}}\cos\left(\frac{\theta}{2}\right)\left[\kappa - 1 + 2\sin^2\left(\frac{\theta}{2}\right)\right] \tag{4}$$

$$u_x^{II} = \frac{K_{II}}{2\mu}\sqrt{\frac{r}{2\pi}}\sin\left(\frac{\theta}{2}\right)\left[\kappa + 1 + 2\cos^2\left(\frac{\theta}{2}\right)\right] \tag{5}$$

$$u_y^I = \frac{K_I}{2\mu}\sqrt{\frac{r}{2\pi}}\sin\left(\frac{\theta}{2}\right)\left[\kappa + 1 - 2\cos^2\left(\frac{\theta}{2}\right)\right] \tag{6}$$

$$u_y^{II} = \frac{K_{II}}{2\mu}\sqrt{\frac{r}{2\pi}}\cos\left(\frac{\theta}{2}\right)\left[\kappa - 1 - 2\sin^2\left(\frac{\theta}{2}\right)\right] \tag{7}$$

$$\kappa = 3 - 4\mu \tag{8}$$

$$\mu = \frac{E}{2(1+\nu)} \tag{9}$$

where κ and μ are the Kolosov constant and shear modulus, respectively.

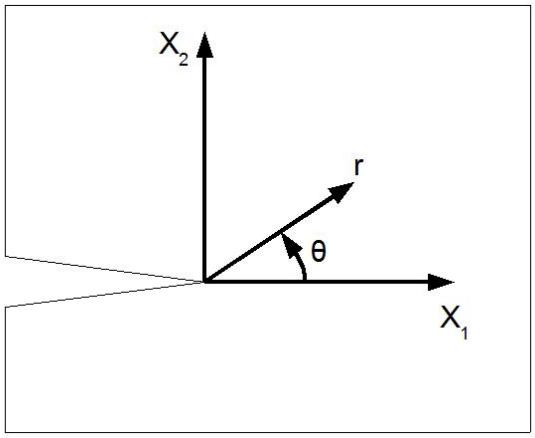

Figure 2: Crack-tip-based coordinate system

It is evident that the above displacement fields (and the corresponding stress fields) are asymptotic in nature. This would imply that the stresses go to infinity as one approaches the crack tip. This, of course, does not occur, but it does go to the heart of the validity of the specimen-independence assumption listed above. The apparent contradiction is resolved as follows.

For a crack in a perfectly elastic material, the asymptotic solution listed in Equations 4 - 7 are expected to become increasingly accurate as one approaches the crack tip. In regions far away from the tip, the fields are influenced by boundary conditions, sample geometry, etc. and therefore do not conform to the asymptotic solution. At the other extreme, when very close to the crack tip, the solution also breaks down - the infinite stresses do not occur at least in part because of material plasticity, a clear violation of the elastic assumption inherent in LEFM.

In between these two cases there exists a region termed the *region of K dominance*, where one is close enough to the crack tip to ignore the specifics of the test specimen but far enough away for the assumptions of linearity and elasticity to still hold. It is within this area that the fields are governed solely by the stress intensity factors. Methods for calculating SIF will be covered in Section 3.6.

Another way of characterizing a crack is to use so-called energy methods. The energy release rate is one such method. It is based on the assumption that, whatever the specifics involved in a particular crack propagation, energy is dissipated. It takes a small amount of energy to create the new free surfaces produced by crack growth. Even if the assumptions of LEFM are violated very near the crack tip (plasticity, etc.), as long as such processes remain constant during propagation, the energy dissipated will also remain constant and may be quantified. The energy release rate is shown below in the Griffith energy balance

$$\frac{dW}{da} - \frac{dU}{da} = \frac{d\Gamma}{da} \tag{10}$$

where W is the external work, U is the elastic energy, Γ is the energy required for crack growth, and a is the length of the crack. When the left hand side is divided by the sample thickness, the energy release rate, G, is obtained. If $G \geq G_c$ then the crack will propagate, with G_c being the fracture toughness of the material.

These two methods may be related to each other by

$$G = \frac{(K_I^2 + K_{II}^2)}{\overline{E}}, \quad \overline{E} = \frac{E}{(1-\nu^2)} \quad \text{(plane strain)} \tag{11}$$

with E and ν denoting the Young's modulus and Poisson's ratio, respectively.

2.2 Interface Fracture Mechanics

A schematic of a crack in a bimaterial system is shown in Figure 3. The crack lies at the interface of the two materials, with material 1 located above the crack and material 2 below. The materials have Young's moduli and Poisson's ratios of E_1 and ν_1, and E_2 and ν_2, respectively.

The stress singularity of the crack tip is now not only determined by the discontinuity across the crack (as in bulk fracture) but also by the strain discontinuity at the interface. Williams [41] was the first to propose analytical solutions for interface fracture problems. He was followed by Rice [29] who clarified the meaning of the

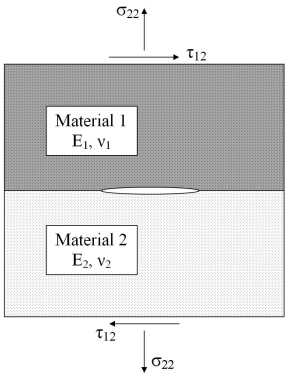

Figure 3: Schematic of a bimaterial crack

complex SIF: the elastic mismatch at a bimaterial crack means that even under pure mode I loading, shear stresses will be produced and there will always exist a mixed mode stress state. Therefore, in interface fracture, the SIFs are denoted by K_1 and K_2 and the in-plane traction vector at a distance r ahead of the crack tip becomes [19]

$$(\sigma_{22} + i\tau_{12})_{\theta=0} = \frac{(K_1 + iK_2)r^{i\epsilon}}{\sqrt{2\pi r}} \tag{12}$$

where ϵ is the bimaterial constant defined below. It should be noted that K_1 and K_2 reduce to the standard K_I and K_{II} when there is no elastic mismatch.

The degree of elastic mismatch between the two materials is characterized by the bimaterial constant, ϵ, which becomes zero when the two materials are the same.

$$\epsilon = \frac{1}{2\pi} \log\left(\frac{1-\beta}{1+\beta}\right) \tag{13}$$

where β is the second Dundurs parameter

$$\beta = \frac{\mu_1(\kappa_2 - 1) - \mu_2(\kappa_1 - 1)}{\mu_1(\kappa_2 + 1) + \mu_2(\kappa_1 + 1)} \tag{14}$$

and μ_i and κ_i are the shear modulus and Kolosov constant, respectively, of material i $(i = 1, 2)$.

The energy release rate is related to the magnitude of the SIF by

$$\mathcal{G} = \frac{1}{E^*} \frac{\mathbf{K}^2}{\cosh^2(\pi\epsilon)}, \ \mathbf{K}^2 = \mathbf{K}\overline{\mathbf{K}} = K_1^2 + K_2^2 \tag{15}$$

where

$$\frac{2}{E^*} = \frac{1}{\overline{E_1}} + \frac{1}{\overline{E_2}}, \quad \overline{E_i} = \frac{E_i}{1-\nu_i^2} \quad \text{(plane strain)} \tag{16}$$

It is known that interface toughness is a function of the direction of loading at the crack tip [39] and therefore the mode angle becomes a very important factor in design. For interface fracture, even when the body is under a pure mode I load, the crack tip will experience a mix of both mode I and mode II loading due to the elastic mismatch between the materials. Also, the stress field about the interface is oscillatory, as seen in Figure 4. This means that the mode angle for an interface crack is not a constant as in bulk fracture; instead, it varies along the interface as can be seen in its dependence on l, the so-called reference length [19]

$$\psi = \tan^{-1}\left(\frac{\mathrm{Im}[\mathbf{K}l^{i\epsilon}]}{\mathrm{Re}[\mathbf{K}l^{i\epsilon}]}\right) \tag{17}$$

While the mode angle depends upon the choice of l, it can be shown from the above equation that $\psi_2 = \psi_1 + \epsilon \ln(l_2/l_1)$ and therefore the mode angle may be easily transformed between values of l.

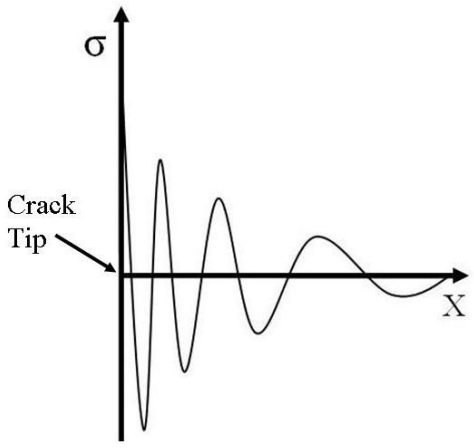

Figure 4: Oscillatory stress field about material interface in front of crack tip

The Cartesian components of the near-tip displacement fields in the upper-half plane are [38]

$$u_j = \frac{1}{2\mu_1}\sqrt{\frac{r}{2\pi}}\left\{\mathrm{Re}\left[\mathbf{K}r^{i\epsilon}\right]\tilde{u}_j^I(\theta,\epsilon,\nu_1) + \mathrm{Im}\left[\mathbf{K}r^{i\epsilon}\right]\tilde{u}_j^{II}(\theta,\epsilon,\nu_1)\right\} \quad (j=1,2) \tag{18}$$

$$\tilde{u}_1^I = A\left[-e^{2\epsilon(\pi-\theta)}\left(\cos\frac{\theta}{2}+2\epsilon\sin\frac{\theta}{2}\right)+\kappa_1\left(\cos\frac{\theta}{2}-2\epsilon\sin\frac{\theta}{2}\right)+\left(1+4\epsilon^2\right)\sin\frac{\theta}{2}\sin\theta\right], \tag{19}$$

$$\tilde{u}_1^{II} = A\left[e^{2\epsilon(\pi-\theta)}\left(\sin\frac{\theta}{2}-2\epsilon\cos\frac{\theta}{2}\right)+\kappa_1\left(\sin\frac{\theta}{2}+2\epsilon\cos\frac{\theta}{2}\right)+\left(1+4\epsilon^2\right)\cos\frac{\theta}{2}\sin\theta\right], \tag{20}$$

$$\tilde{u}_2^I = A\left[e^{2\epsilon(\pi-\theta)}\left(\sin\frac{\theta}{2}-2\epsilon\cos\frac{\theta}{2}\right)+\kappa_1\left(\sin\frac{\theta}{2}+2\epsilon\cos\frac{\theta}{2}\right)-\left(1+4\epsilon^2\right)\cos\frac{\theta}{2}\sin\theta\right], \tag{21}$$

$$\tilde{u}_2^{II} = A\left[e^{2\epsilon(\pi-\theta)}\left(\cos\frac{\theta}{2}+2\epsilon\sin\frac{\theta}{2}\right)-\kappa_1\left(\cos\frac{\theta}{2}-2\epsilon\sin\frac{\theta}{2}\right)+\left(1+4\epsilon^2\right)\sin\frac{\theta}{2}\sin\theta\right] \tag{22}$$

where

$$A = \frac{e^{-\epsilon(\pi-\theta)}}{\left(1+4\epsilon^2\right)\cosh(\pi\epsilon)} \tag{23}$$

and r and θ are shown in Figure 2. For the displacement fields in the lower-half plane (material 2), replace $\pi\epsilon$ by $-\pi\epsilon$.

CHAPTER III

THE EXTENDED FINITE ELEMENT METHOD

3.1 Introduction

The Finite Element Method (FEM) has been at the forefront of the computer-modeling revolution of recent decades. When it comes to analyzing layered materials, though, it has a relative blind spot. It can model the behavior within individual layers quite well, but it encounters great difficulty when looking at interfaces between layers, that is, the area most critical to a composite material. The standard FEM requires extremely fine meshes in the region of such interfaces - especially when discontinuities such as fractures or voids are present - in addition to the mesh having to conform to the various discontinuities. In some case, even the finest mesh cannot produce an accurate result. A clear example of this was shown in a study on channel-cracking of thin films [16]: the FEM mesh had elements that were *7 orders of magnitude* smaller than those used by the XFEM mesh, yet still failed to produce results as accurate.

Several approaches have been taken to attempt to overcome these difficulties, among them singular elements [18] and "meshless" methods. Both require considerable modification of existing finite element codes; they are oftentimes more trouble than they're worth.

The XFEM does not suffer from this significant drawback [3]; it is only an addition to the FEM, whose foundations remain untouched. The touchstone of the XFEM is its ability to incorporate *a priori* knowledge of a model's response (to, say, discontinuities) into the analysis itself. The use of the Partition of Unity Method allows the behavior of interest to be known throughout the element - not just at the nodes - and, hence, the mesh need not align to boundaries/discontinuities.

3.2 Partition of Unity Method

In the finite element method, a basis function, N_I, is associated with with a node I. The region of support of a basis, or shape, function is the set of elements that include node I. These shape functions form a partition of unity

$$\sum_{I \in \mathcal{N}} N_I(\mathbf{x}) = 1 \tag{24}$$

It follows that any arbitrary function $\Upsilon(\mathbf{x})$ may be reproduced exactly by

$$\sum_{I \in \mathcal{N}} N_I(\mathbf{x}) \Upsilon(\mathbf{x}) = \Upsilon(\mathbf{x}) \tag{25}$$

It is this ability that forms the basis of the XFEM. By appropriately choosing the function $\Upsilon(\mathbf{x})$ for each node, *a priori* knowledge of of a model's behavior may be incorporated while retaining the firm mathematical basis of standard finite element analysis.

3.3 Bulk Fracture Modeling

In isotropic linear elastic fracture analysis, two sets of functions are used to handle the presence of a crack: a discontinuous function for the crack line and a set of asymptotic functions for the crack tip. Let the interior of the crack surface be denoted by Γ and the crack tip by Λ. The set of all nodes is $\mathcal{N}$; nodes whose support is cut by the crack tip is $\mathcal{N}_\Lambda$; and those nodes whose support is cut by the crack line are denoted by $\mathcal{N}_\Gamma$ ($\mathcal{N}_\Lambda \cap \mathcal{N}_\Gamma$=0) [37] The enriched displacement approximation then becomes [25]

$$\mathbf{u}^h(\mathbf{x}) = \sum_{I \in \mathcal{N}} N_I(\mathbf{x}) \left[\mathbf{u}_I + \underbrace{H(\mathbf{x})\mathbf{a}_J}_{J \in \mathcal{N}_\Gamma} + \underbrace{\sum_{\alpha=1}^{4} \Phi_\alpha(\mathbf{x}) \mathbf{b}_K^\alpha}_{K \in \mathcal{N}_\Lambda} \right] \tag{26}$$

where $\mathbf{u}_I$ is the nodal displacement vector of the continuous part of the finite element solution, $\mathbf{a}_J$ is the nodal enriched degree of freedom vector of the discontinuous crack line function, and $\mathbf{b}_K^\alpha$ are the nodal enriched degree of freedom vectors of the asymptotic crack tip. The literature is silent on the physical meaning of $\mathbf{a}_J$ and $\mathbf{b}_K^\alpha$, but

they may be viewed as the amount of "displacement" caused by the crack line and tip, respectively. The modified Heaviside function associated with the crack line is

$$H(\mathbf{x}) = \begin{cases} +1 & \text{if } (\mathbf{x} - \mathbf{x}^*) \cdot \mathbf{n} \geq 0 \\ -1 & \text{otherwise} \end{cases} \tag{27}$$

where $\mathbf{x}$ is a sample (integration) point, $\mathbf{x}^*$ is the projection of $\mathbf{x}$ onto the crack surface, and $\mathbf{n}$ is the unit outward normal to the crack at $\mathbf{x}^*$. The asymptotic functions associated with the crack tip are

$$[\Phi_\alpha(\mathbf{x}), \alpha = 1 - 4] = \left[\sqrt{r} \sin \frac{\theta}{2}, \sqrt{r} \cos \frac{\theta}{2}, \sqrt{r} \sin \frac{\theta}{2} \sin \theta, \sqrt{r} \cos \frac{\theta}{2} \sin \theta \right] \tag{28}$$

Figure 5 shows the type of enrichment active on each node in an isotropic fracture model.

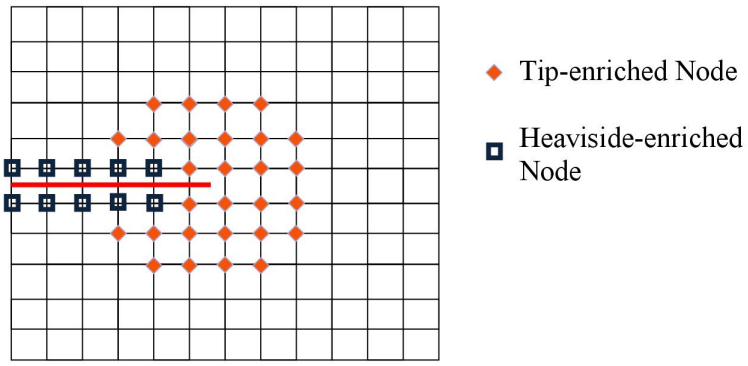

Figure 5: Nodal enrichment scheme for bulk fracture

3.4 Interface Modeling

In the standard finite element method, a material interface must align with the mesh. This increases the time spent on pre-processing, especially when the model contains a large number of complex interfaces. Just as XFEM elements can handle the displacement discontinuity across a crack line, they are also able to cope with the strain discontinuity across an interface, greatly reducing model preparation time.

Many enrichment functions have been proposed to account for the interface strain discontinuity. Since strain is the derivative of displacement, and the strain is discontinuous across the interface, all that is needed is a function that has a discontinuous derivative. The simplest method, shown in Figure 6 as F_1, uses the absolute value of the signed distance function [21]. The approach used in the current work, F_2 in Figure 6, is a slight modification of the above - the main advantage being that the function goes to zero at the enriched nodes, resulting in an improvement of the accuracy of the model [28]

$$\Psi(\mathbf{x}) = \sum_I N_I(\mathbf{x}) \left|\Psi_I\right| - \left|\sum_I N_I(\mathbf{x})\Psi_I\right| \tag{29}$$

where Ψ_I is the signed distance of node I to the interface. With the interface denoted by Π, this then allows the displacement approximation to take the form

$$\mathbf{u}^h(\mathbf{x}) = \sum_{I\in\mathcal{N}} N_I(\mathbf{x}) \left[\mathbf{u}_I + \underbrace{\Psi(\mathbf{x})\mathbf{c}_L}_{L\in\mathcal{N}_\Pi}\right] \tag{30}$$

where c_L is the nodal enriched degree of freedom vector of the interface signed distance function and $\mathcal{N}_\Pi$ is the set of nodes whose support is cut by the interface.

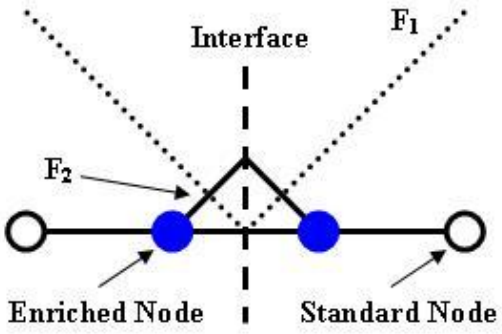

Figure 6: 1D example of functions used to model material interface

When an interface cuts through an element, there naturally exists two materials within the same element. A sampling algorithm, utilizing the signed distance function, determines which material exists at a sampling point and assigns material properties

accordingly. If the interface happens to align with the mesh, there is no need for the above enrichment (though material sampling is still necessary) and the system behaves as it would in a standard finite element model.

3.5 Interface Fracture Modeling

As one might expect, the displacement approximation for interface fracture is basically a combination of those used for interface modeling and bulk fracture. The Heaviside function continues to account for the crack line, the interface is still modeled with the modified signed distance function, but the asymptotic functions must be modified to represent the behavior of a crack tip between two dissimilar materials. The new functions follow from Equations 18-23 [38]

$$\begin{aligned}[\Phi_\alpha(\mathbf{x}), \alpha = 1-12] = \Bigg[& \sqrt{r}\cos(\epsilon \log r)e^{-\epsilon\theta}\sin\frac{\theta}{2}, \sqrt{r}\cos(\epsilon \log r)e^{-\epsilon\theta}\cos\frac{\theta}{2}, \\ & \sqrt{r}\cos(\epsilon \log r)e^{\epsilon\theta}\sin\frac{\theta}{2}, \sqrt{r}\cos(\epsilon \log r)e^{\epsilon\theta}\cos\frac{\theta}{2}, \\ & \sqrt{r}\cos(\epsilon \log r)e^{\epsilon\theta}\sin\frac{\theta}{2}\sin\theta, \sqrt{r}\cos(\epsilon \log r)e^{\epsilon\theta}\cos\frac{\theta}{2}\sin\theta, \\ & \sqrt{r}\sin(\epsilon \log r)e^{-\epsilon\theta}\sin\frac{\theta}{2}, \sqrt{r}\sin(\epsilon \log r)e^{-\epsilon\theta}\cos\frac{\theta}{2}, \\ & \sqrt{r}\sin(\epsilon \log r)e^{\epsilon\theta}\sin\frac{\theta}{2}, \sqrt{r}\sin(\epsilon \log r)e^{\epsilon\theta}\cos\frac{\theta}{2}, \\ & \sqrt{r}\sin(\epsilon \log r)e^{\epsilon\theta}\sin\frac{\theta}{2}\sin\theta, \sqrt{r}\sin(\epsilon \log r)e^{\epsilon\theta}\cos\frac{\theta}{2}\sin\theta \Bigg] \end{aligned} \tag{31}$$

This then allows the displacement approximation to be written

$$\mathbf{u}^h(\mathbf{x}) = \sum_{I\in\mathcal{N}} N_I(\mathbf{x}) \Bigg[\mathbf{u}_I + \underbrace{H(\mathbf{x})\mathbf{a}_J}_{J\in\mathcal{N}_\Gamma} + \underbrace{\sum_{\alpha=1}^{12} \Phi_\alpha(\mathbf{x})\mathbf{b}_{\alpha K}}_{K\in\mathcal{N}_\Lambda} + \underbrace{\Psi(\mathbf{x})\mathbf{c}_L}_{L\in\mathcal{N}_\Pi} \Bigg] \tag{32}$$

The nodal enrichment scheme can be seen in Figure 7 for an interface fracture aligned with the mesh and in Figure 8 for an arbitrarily-aligned interface fracture. It will be noted that in Figure 8, while a tip-enriched node will also be enriched by the interface functions, Heaviside-enriched nodes are not. This stems from the fact

that elements along the crack line are completely cut - the displacement discontinuity renders the strain discontinuity unnecessary.

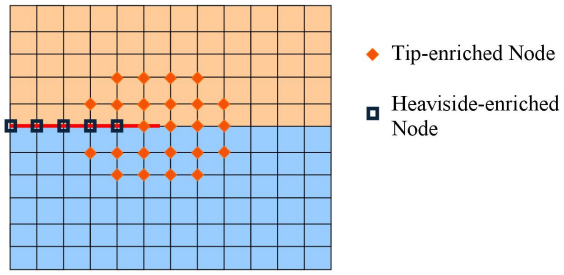

Figure 7: Nodal enrichment scheme for (mesh-aligned) interface fracture

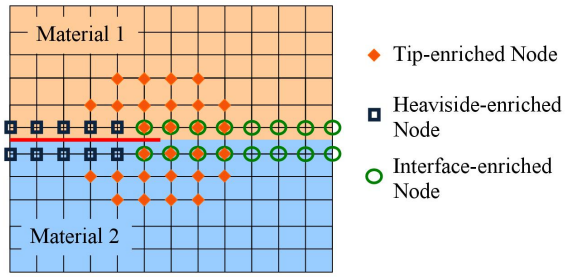

Figure 8: Nodal enrichment scheme for (arbitrarily-aligned) interface fracture

3.6 Stress Intensity Factor Evaluation

Knowledge of the displacements, strains, and stresses of a fracture model is useful, especially when interpreted by a post-processing program. However, these measures of a model's response consist of large amounts of tabulated data which are difficult to grasp as a whole. Stress intensity factors (SIFs) condense such data into an easily understood form and, as such, lend themselves more readily to analysis and design.

Numerous techniques have been developed to compute SIFs, such as the Displacement Extrapolation method, the Virtual Crack Extension method, and the interaction integral method. The last of these is used in the current work - specifically, the domain form of the contour interaction integral [30].

The interaction integral consists of superimposing auxiliary fields onto the actual fields produced by the solution of the boundary value problem. When the auxiliary fields are chosen in the proper form, the general 2D crack tip contour integral may be transformed into the contour interaction energy integral

$$I = \int_{\Gamma} (\sigma_{ik}\varepsilon_{ik}^{aux}\delta_{1j} - \sigma_{ij}u_{i,1}^{aux} - \sigma_{ij}^{aux}u_{i,1})n_j d\Gamma \tag{33}$$

where u_i^{aux}, ε_{ik}^{aux}, and σ_{ij}^{aux} are the auxiliary displacement, strain, and stress fields, respectively. The domain form of this interaction integral changes the evaluation of a line integral into the calculation of an integral over an area - a technique ideally suited to a finite element framework

$$I = -\int_{A} (\sigma_{ik}\varepsilon_{ik}^{aux}\delta_{1j} - \sigma_{ij}u_{i,1}^{aux} - \sigma_{ij}^{aux}u_{i,1})q_{,j} dA \tag{34}$$

where q is a smooth scalar weighting function that is unity at the crack tip and becomes zero at the edge of the domain area. Based on Equation 15, the interaction integral can be related to the SIFs as follows

$$I = \frac{2}{E^* \cosh^2(\pi\epsilon)}[K_1 K_1^{aux} + K_2 K_2^{aux}] \tag{35}$$

where K_1^{aux} and K_2^{aux} are the auxiliary SIFs for the chosen auxiliary fields. With $K_1^{aux} = 1$, $K_2^{aux} = 0$, and with $I = I_1$, K_1 may be calculated (a similar method is used for K_2)

$$K_1 = \frac{E^* \cosh^2(\pi\epsilon)}{2} I_1, \;\; K_2 = \frac{E^* \cosh^2(\pi\epsilon)}{2} I_2 \tag{36}$$

In this work, the form of the auxiliary fields used are those given in [24].

CHAPTER IV

ABAQUS-SPECIFIC IMPLEMENTATION

4.1 Nodal Degrees of Freedom

One of the major hallmarks of the XFEM is its increased number of degrees of freedom per node. In a stand-alone code, this poses no problem, as the extra dofs are easily added to the stiffness and force matrices by simply increasing their dimensions. Such an approach is not possible within Abaqus, however, because the user does not have direct access to either the global stiffness or force matrices, nor does a user directly define the dofs at each node. At first, this was not seen as a problem, as Abaqus supplies the user access to "free" nodal dofs during element connectivity definition in the input file. By querying both the Abaqus Documentation and the Support Center, it was believed that there were an unlimited number of "free" dofs to work with.

This turned out to be false. It was found that only 20 "free" dofs were available per node. This was not an issue for the homogeneous phase of the research since only 12 were needed (2 for displacement, 2 for the crack line, and 8 for the crack tip). Issues arose only when the interface code attempted to utilize 30 dofs/node (2 for displacement, 2 for the crack line, 2 for the interface, and 24 for the crack tip). The solution came when it was realized that extra nodes, including dofs, could be added to the user element. Initially, there was concern that these extra nodes would greatly complicate the analysis by essentially creating 2 partial models that would then have to be integrated somehow at the end of the simulation.

Fortunately, this too turned out to be false. The "free" dofs from the extra nodes could be "borrowed" and used just like the "free" dofs from the standard nodes, combining to provide the requisite 30. Nothing else need then be done about

the extra, or "phantom", nodes - they were assigned no displacement or any other physical variables and so became, in effect, just extra storage space for the physical nodes with no reflection in reality.

Figure 9 shows a schematic of the element. The phantom nodes were defined to be coincident to the corresponding standard nodes for ease of bookkeeping, though since they lack physicality, each could have been defined at the origin (or any other set of coordinates). The standard nodes were assigned 16 dofs, while the phantom nodes provided 14 dofs each.

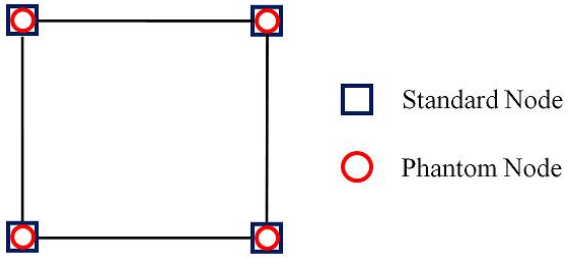

Figure 9: Schematic of user element nodes

4.2 User Element Information Flow

Figure 10 shows the information flow through the Abaqus user element. In most respects, it follows the same general steps as a standard finite element. The additions that make it an XFEM element are highlighted in red; these will be discussed in greater depth than the standard steps.

The input file defines the analysis and contains:

- Nodal coordinates (both standard and phantom)
- Location of crack line, crack tip, and material interfaces
- Linearly elastic material properties for material(s) used
- Degree of freedom assignments for all nodes

- Element connectivity and type (in the present case, the XFEM user element)
- Nodal boundary conditions

The two loops of Figure 10 correspond to the two steps needed for the analysis. The first step is the familiar one of assembling and solving the global stiffness and force matrices to determine nodal displacements/forces (also element stresses and strains). Once this is completed, the second step takes the information from the first step and calculates the stress intensity factors for the model.

The first step starts by considering element 1. Several geometry-based subroutines determine if the element is affected by the crack line, crack tip, or material interface and, if so, the element is partitioned (via Delaunay triangulation) as necessary to make it piecewise-continuous. The various enrichments (if any) found for each of the element's nodes are noted for future use and the locations of integration points found.

The user element then loops through each of the element's integration points. If the element has no enriched nodes, the standard FEM displacement B-matrix is calculated so the stresses and strains may be computed and the integration point's contribution to the element-level stiffness and force matrices found. If there are *any* enrichments on any of the nodes, the standard FEM B-matrix is still calculated, but so are *all* of the enriched B-matrices (for crack line, crack tip, and material interface). The unused enriched B-matrices are zeroed out, node by node, and those that remain are used as before to find stresses, strains, and the contributions to the stiffness and force matrices.

Once all of an element's integration points have been analyzed, the user element sums all the contributions to the element stiffness and force matrices and passes this data to Abaqus. The same procedure is then carried out on the next element, etc. until all elements have been seen. Abaqus then assembles and solves the global $Ku{=}f$ equation.

The second step begins, as the first, with element 1. It first checks to see if the element is in one of the defined contours that will be used to calculate the SIFs. If is not, Abaqus moves on to the next element. Once it finds an element located in a contour, the user element retrieves the integration point locations from the first step. The points are looped through and the stresses, strains, and displacements recovered from before. These values are then used to calculate the integration point's contribution to the element's interaction integral value. This process is repeated for all integration points in all contour elements. When all of the necessary elements have been processed, the resulting data is used to compute the stress intensity factors for the model. The simulation's final act is to output the nodal displacements, nodal reaction forces, and SIFs to a results file. The analysis is complete.

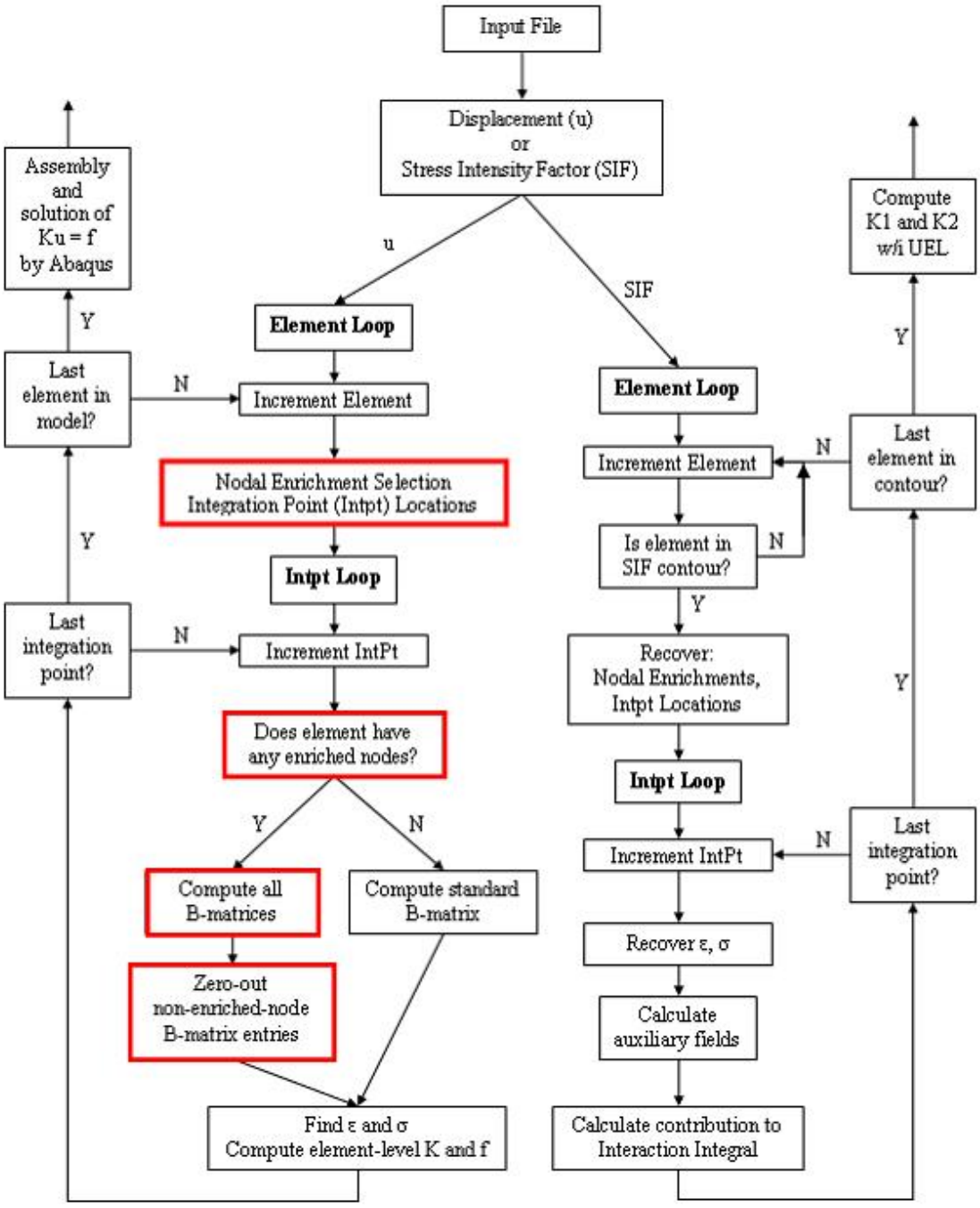

Figure 10: Flow of information through Abaqus user element

CHAPTER V

RESULTS

5.1 Stress Intensity Factor Validation

As will be shown, the SIFs for the interface benchmark are not correct. There are two possible explanations for this: either the user element is passing the wrong values to the SIF subroutine, or there is an error in the SIF subroutine itself. To rule out the latter, a simple test is used to validate the SIF calculations [37].

The model consists of a bimaterial single edge notched tension specimen (the same as shown in Figure 19). Equations 18-23 are used to define the near-tip displacement field on the boundary of the specimen. For simplicity's sake, K_1 and K_2 are both set to 1, $E_1 = 10$, $E_2 = 1$, and $\nu_1 = \nu_2 = 0.3$. Several mesh densities were used and the resulting SIFs were compared to the reference values of 1. For all meshes, the computed K_1 and K_2 both had less than one percent error, similar to the results of [37].

Therefore, the problem is not with the SIF calculations, but resides in the user element. This issue will be discussed further in Chapter 6.

5.2 Homogeneous Structure Benchmarks

Results from the XFEM model are compared to two common benchmarks with closed-form solutions, the single edge notched tension and the center cracked tension specimens. Good agreement between the XFEM and analytical solutions is shown.

5.2.1 Single Edge Notched Tension Plate (SENT)

The benchmark setup is shown in Figure 11. A crack of length a is located at the left edge and along the midline of a W x H plate. A uniform tensile stress of σ is

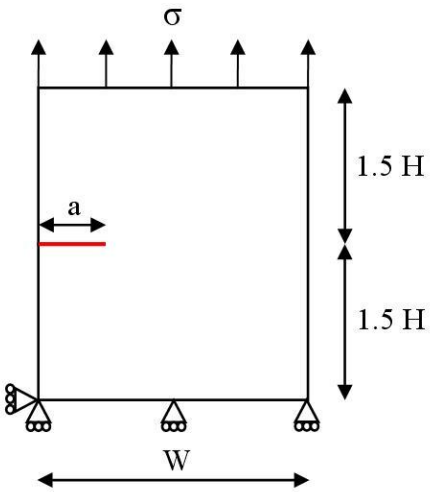

Figure 11: Boundary conditions and dimensions of a homogeneous SENT specimen

applied to the top edge, while the lower left corner is pinned and the bottom edge is constrained in the vertical direction. The mesh density, the plate dimensions, and the crack length are all varied to assess the effect on the model's accuracy.

The effect of mesh density, characterized by elements per unit length h_e, is studied first. Plate dimensions of $W = 10$ and $H = 30$, and a crack length of $a/W = 1/4$ are used. Since the plate is in pure mode I loading, K_{II} should equal zero and K_I is given by Ewalds and Wanhill [11] for a finite SENT plate

$$K_I = C\sigma\sqrt{a\pi} \tag{37}$$

where

$$C = 1.122 - 0.231(a/W) + 10.550(a/W)^2 - 21.710(a/W)^3 + 30.382(a/W)^4 \tag{38}$$

The effect of crack-mesh alignment is also considered for three possible cases: the crack line and tip align to the mesh, only the crack line is aligned to the mesh, and neither the crack line nor the crack tip align to the mesh. All error results are shown in Table 1 and were computed by

$$K_i^{error} = \frac{K_i^{simulation} - K_I^{reference}}{K_I^{reference}} \tag{39}$$

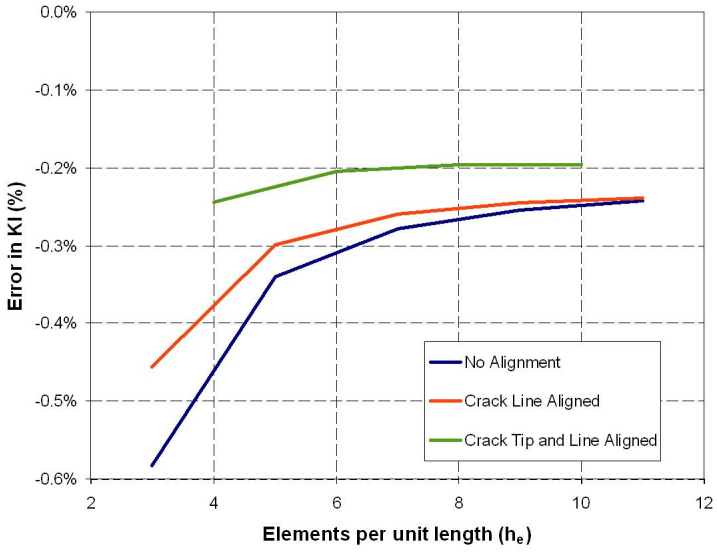

Figure 12: Influence of mesh density / alignment on SIF accuracy for homogeneous SENT specimen

Table 1: Influence of mesh density / alignment on SIF accuracy for homogeneous SENT specimen

h_e	K_I	Error	K_{II}	Error
No Alignment				
3	418192861	-0.583%	-537	-0.00013%
5	419214205	-0.340%	-540	-0.00013%
7	419474929	-0.278%	-540	-0.00013%
9	419574851	-0.254%	-542	-0.00013%
11	419621540	-0.243%	-543	-0.00013%
Crack Line Aligned				
3	418725530	-0.456%	616	0.00015%
5	419387255	-0.299%	-41	-0.00001%
7	419548733	-0.260%	-56	-0.00001%
9	419611496	-0.245%	-171	-0.00004%
11	419639974	-0.239%	-244	-0.00006%
Crack Line and Crack Tip Both Aligned				
4	419620220	-0.243%	-999	-0.00024%
6	419786626	-0.204%	-782	-0.00019%
8	419815046	-0.197%	-696	-0.00017%
10	419815050	-0.197%	-673	-0.00016%

As can be seen, the XFEM results agree very well with the theoretical values, even with a relatively coarse mesh. Figure 12 shows that full alignment of the crack with the mesh produces the best results, even at higher mesh densities as the other two groups converge. This is thought to be a function of having the crack tip located on a node, as this only occurs in the full alignment case.

Next is shown the influence of the plate aspect ratio, H/W, on the SIF calculations. The width of the plate is $W = 10$, the crack length is $a/W = 1/4$, a mesh density of $h_e = 9$ is used, and H is varied from 10 to 60. Equation 37 is again used as the reference value.

Figure 13 shows the relative errors in K_I and K_{II}. A dramatic reduction in the measured error can be seen around an H/W of 1.5, but it must also be kept in mind that the error, even in a square specimen, is less than 5 percent. This deviation of the XFEM prediction from theory at low aspect ratios is most likely due to the fact that the applied stress can no longer be considered "far-field" and Equation 37 begins to lose validity.

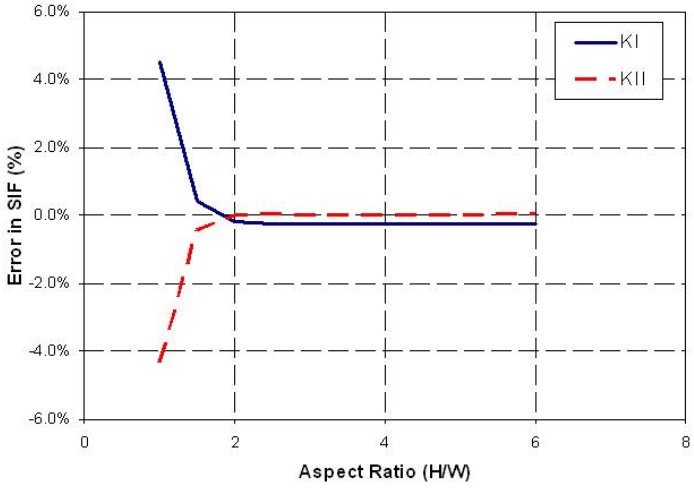

Figure 13: Influence of aspect ratio on SIF accuracy for homogeneous SENT specimen

Finally, the accuracy of the XFEM model is gauged when the normalized crack length, a/W, is varied. Model dimensions are $W = 10$ and $H = 30$, mesh density is $h_e = 9$, and the crack length ranges from 1.50 to 5.06. The values of a/W are nonuniform due to a decision to keep the crack and mesh misaligned.

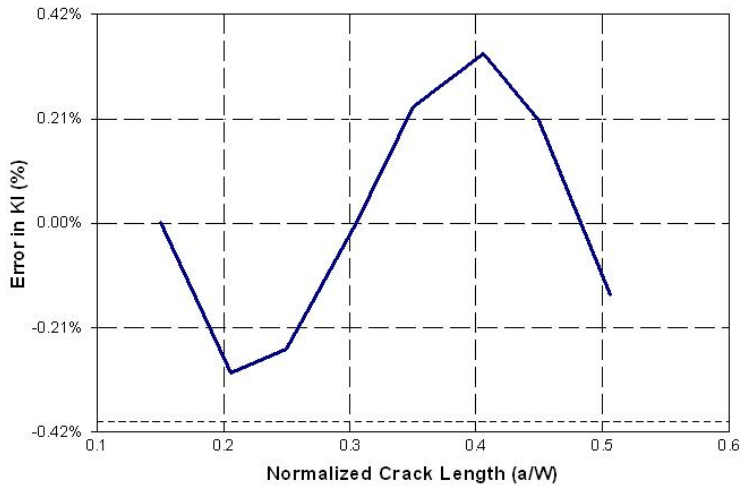

Figure 14: Influence of crack length on SIF accuracy for homogeneous SENT specimen

Again, very good agreement between Equation 37 and the XFEM is achieved. Figure 14 shows the results. It is not known why the K_I error seems to oscillate about zero and nothing in the literature suggests that such should occur. One possibility, with the errors so small, is that it is simply numerical noise, or most likely, an artifact of the coding.

5.2.2 Center Crack Tension Plate (CCT)

The benchmark setup is shown in Figure 15. A crack of length $2a$ is centered about the vertical and horizontal midlines of a W x H plate. A uniform tensile stress of σ is applied to the top edge, while the lower left corner is pinned and the bottom edge is constrained in the vertical direction. The mesh density, the plate dimensions, and

the crack length are all varied to assess the effect on the model's accuracy.

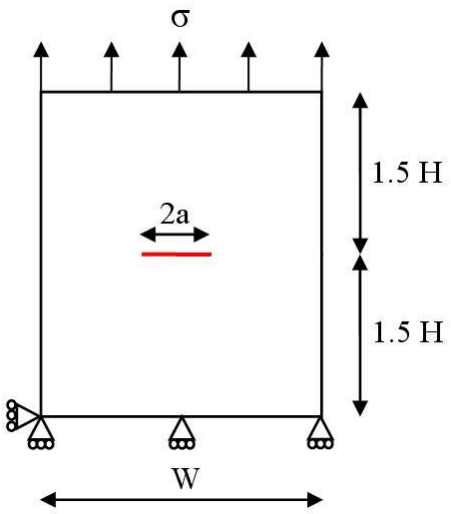

Figure 15: Boundary conditions and dimensions of a homogeneous CCT specimen

The effect of mesh density, characterized by elements per unit length h_e, is studied first. Plate dimensions of $W = 10$ and $H = 30$ and a half crack length of $a/W = 0.15$ are used. Since the plate is in pure mode I loading, K_{II} should equal zero and K_I is given by Ewalds and Wanhill [11] for a finite CCT plate

$$K_I = C\sigma\sqrt{a\pi} \tag{40}$$

where

$$C = 1 + 0.256(a/W) - 1.152(a/W)^2 + 12.200(a/W)^3 \tag{41}$$

The effect of crack-mesh alignment is also considered for three possible cases: the crack line and tip align to the mesh, only the crack line is aligned to the mesh, and the crack line and tip do not align to the mesh. All error results are with regard to Equation 40 and are shown in Table 2.

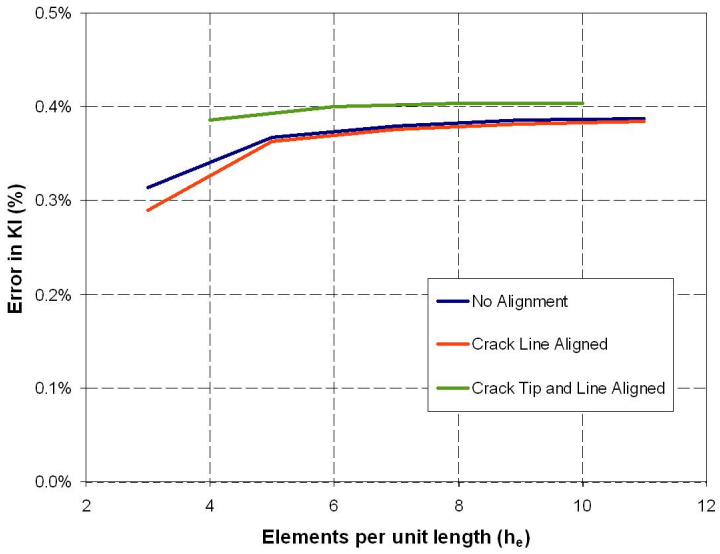

Figure 16: Influence of mesh density / alignment on SIF accuracy for homogeneous CCT specimen

Table 2: Influence of mesh density / alignment on SIF accuracy for homogeneous CCT specimen

h_e	K_I	Error	K_{II}	Error
No Alignment				
3	229444232	0.313%	-140	-0.00006%
5	229566871	0.367%	-129	-0.00006%
7	229594828	0.379%	-131	-0.00006%
9	229609491	0.385%	-128	-0.00006%
11	229613485	0.387%	-131	-0.00006%
Crack Line Aligned				
3	229391059	0.290%	291020	0.12723%
5	229558827	0.363%	82418	0.03603%
7	229588036	0.376%	50448	0.02206%
9	229600233	0.381%	28278	0.01236%
11	229607179	0.384%	19938	0.00872%
Crack Line and Crack Tip Both Aligned				
4	229611460	0.386%	156727	0.06852%
6	229643739	0.400%	21233	0.00928%
8	229650564	0.403%	14060	0.00615%
10	229651586	0.404%	10069	0.00440%

Figure 16 shows that, unlike the SENT specimen, the full-alignment case gives the least accurate results, though the other two cases seem to approach its value with increasing mesh density. This seems to suggest that the reference value is slightly too low or, more likely, the code is aiming too high. If this is indeed the case, then the results mirror those of the SENT specimen.

The influence of the plate aspect ratio, H/W, on the SIF calculations is presented next. The width of the plate is $W = 10$, the half crack length is $a/W = 0.15$, a mesh density of $h_e = 9$ is used, and H is varied from 10 to 60. Equation 40 is again used as the reference value.

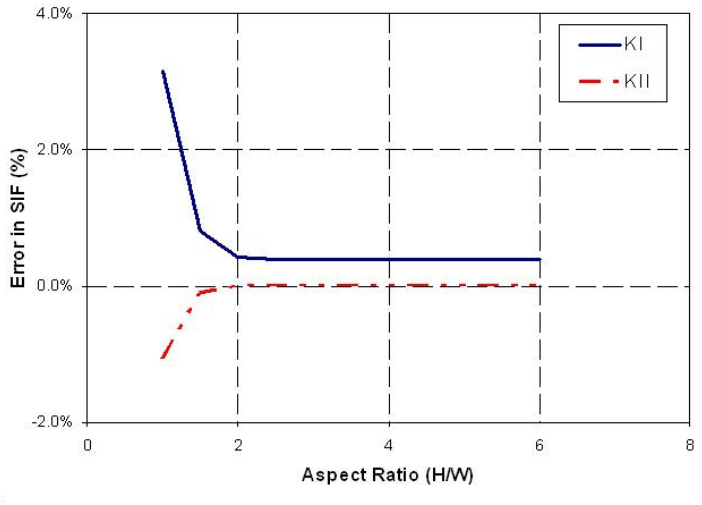

Figure 17: Influence of aspect ratio on SIF accuracy for homogeneous CCT specimen

Figure 17 shows the relative errors in K_I and K_{II}. The trends observed are the same as those for the SENT specimen, except that K_I, instead of dropping slightly below K_{II}, settles slightly above. Regardless, after an aspect ratio of $H/W = 1.5$, the error is less than 1 percent. Again, the deviation from theory at low aspect ratios is most likely due to the decreased validity of "far-field" assumptions.

The last analysis performed on the CCT specimen concerns the accuracy of the

XFEM model when the normalized crack length, a/W, is varied. Model dimensions are $W = 10$ and $H = 30$, mesh density is $h_e = 9$, and the half crack length ranges from $a = 1.50$ to 3.5. The values of a/W are not quite uniform because of a choice to not allow the crack tip to become aligned to the mesh.

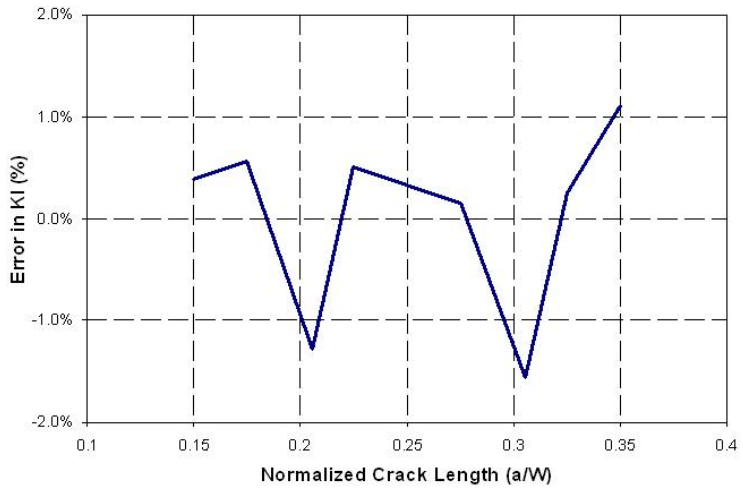

Figure 18: Influence of crack length on SIF accuracy for homogeneous CCT specimen

Once again, very good agreement between Equation 40 and the XFEM is seen. Figure 18 shows the results. As for the SENT model, the K_I error seems to oscillate about zero, but the CCT error is roughly four times as large, though still under 2%. As before, it is either numerical noise or an artifact of the coding.

5.3 Interface Benchmarks

5.3.1 Problems with Interface Implementation

As will be seen, the values for K_I and K_{II} are approximately 20% and 100% too large, respectively. These errors are too large to allow the interface fracture work to be used in a predictive manner; only results for a single edge notched tension plate will be shown to give an idea of the implementation's behavior. However, the stability

of the results (though stable about an incorrect value) suggests that the problem lies somewhere in the roughly 5000 lines of FORTRAN code of the user element, and is not due to a fundamental flaw in the overall approach. Chapter 6 will discuss the matter more fully.

5.3.2 Single Edge Notched Tension Plate (SENT)

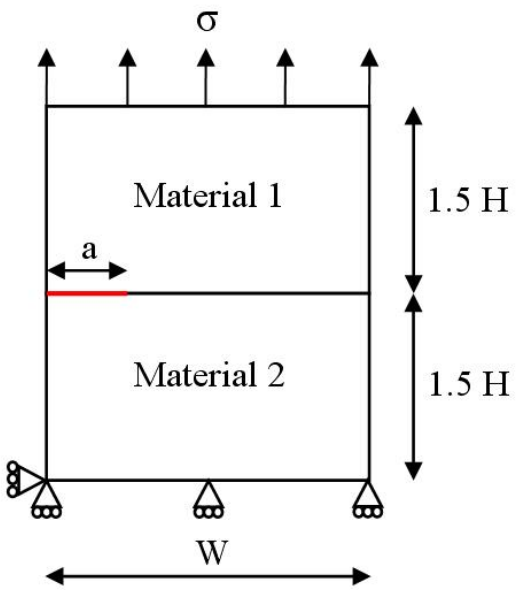

Figure 19: Boundary conditions and dimensions of a interface SENT specimen

Figure 19 shows the benchmark setup. The plate is composed of two materials with their interface located at the midline of the specimen. A crack of length a is located at the left edge and along the interface of the W x H plate. A uniform tensile stress of σ is applied to the top edge, while the lower left corner is pinned and the bottom edge is constrained in the vertical direction. The mesh density, the plate dimensions, and the crack length are all varied to assess the effect on the model's accuracy. The elastic mismatch E_1/E_2 was set to 10 for all models.

The effect of mesh density, characterized by elements per unit length h_e, is studied first. Plate dimensions of $W = 10$ and $H = 30$ and a crack length of $a/W = 1/4$

are used. Unlike the homogeneous specimens, even though the plate is in pure mode I loading the elastic mismatch at the crack tip will cause K_2 to be non-zero. The values of the stress intensity factors are given by Ewalds and Wanhill [11] for a finite bimaterial SENT plate

$$K_1 + iK_2 = C\sigma\sqrt{a\pi}(1 + 2i\epsilon)(2a)^{-i\epsilon} \tag{42}$$

where

$$C = 1.12 - 0.231(a/W) + 10.55(a/W)^2 - 21.72(a/W)^3 + 20.39(a/W)^4 \tag{43}$$

The effect of crack-mesh alignment is also considered for three possible cases: the crack line and tip align to the mesh, only the crack line is aligned to the mesh, and the crack line and tip do not align to the mesh. All error results are with regard to Equation 42 and are shown in Table 3.

Table 3: Influence of mesh density / alignment on SIF accuracy for interface SENT specimen

h_e	K_1	Error	K_2	Error
No Alignment				
3	603658963	43.7%	-89514546	118%
5	527013669	25.5%	-82286748	101%
7	497381740	18.4%	-80559069	96%
9	481491375	14.6%	-79651156	94%
Crack Line Aligned				
3	482978670	15.0%	-83660379	104%
5	466331389	11.0%	-85108087	108%
7	486327539	15.8%	-82725825	102%
9	472674644	12.5%	-84117305	105%
Crack Line and Crack Tip Both Aligned				
4	483037545	15.0%	-87115051	112%
6	476869759	13.5%	-83745038	104%
8	465555109	10.8%	-82540511	101%
10	458075522	9.1%	-81597282	99%

The results for K_1 are more accurate than those of K_2, a trend which was observed in other researchers' results [3] [26], though not to such a large degree. The issue of

alignment also differs between the SIFs: Figure 20 shows that full alignment of the crack with the mesh produces the best results for K_1, while no alignment is best for K_2.

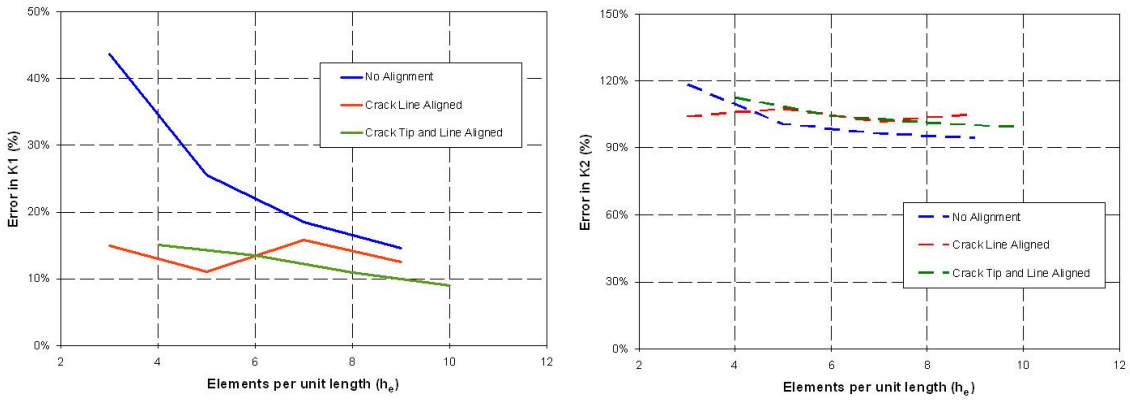

Figure 20: Influence of mesh density / alignment on SIF accuracy for interface SENT specimen

The influence of the plate aspect ratio, H/W, on the SIF calculations is shown next. The width of the plate is $W = 10$, the crack length is $a/W = 1/4$, a mesh density of $h_e = 9$ is used, and H is varied from 10 to 60. Equation 42 is again used as the reference value.

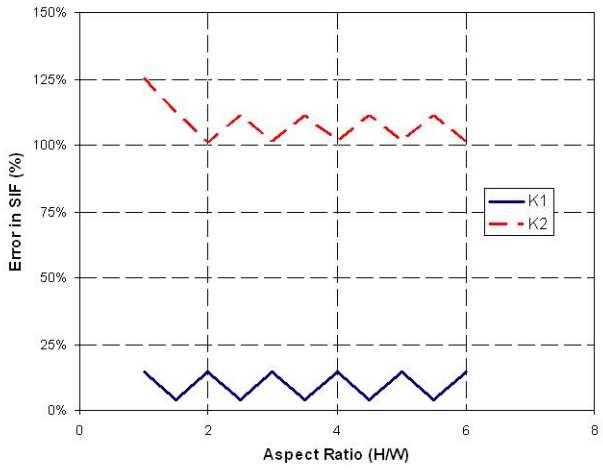

Figure 21: Influence of aspect ratio on SIF accuracy for interface SENT specimen

Figure 21 shows the relative errors in the SIFs . Both results oscillate about a given value, with K_1 again being more accurate than K_2. It is also observed that the oscillations are oppositely phased: K_1 peaks when K_2 is at it's low point, and vice versa. The cause of this phenomenon is unclear, though it may be due to the locations of the SIF contours and reflects the oscillatory nature of the stress field shown in Figure 4.

Lastly, the accuracy of the XFEM model is measured when the normalized crack length, a/W, is varied. Model dimensions are $W = 10$ and $H = 30$, mesh density is $h_e = 9$, and the crack length ranges from 1.50 to 5.06. The values of a/W are, again, not quite uniform because of a choice to keep the crack tip unaligned to the mesh.

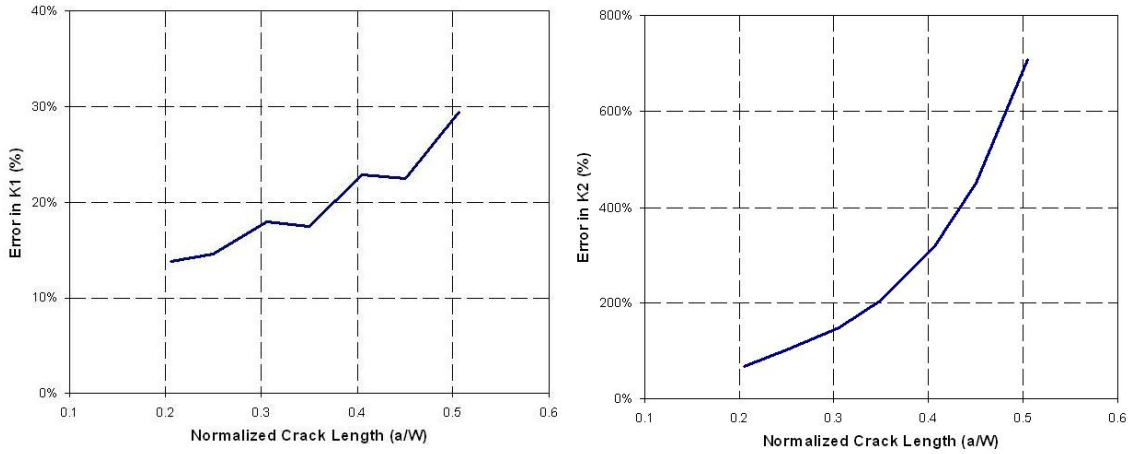

Figure 22: Influence of crack length on SIF accuracy for interface SENT specimen

Figure 22 illustrates the errors in K_1 and K_2, both of which climb almost exponentially with increasing crack length. Several factors may contribute to this, including the higher stress levels caused by a longer crack and/or the invalidation of "far-field" assumptions used in the reference solution.

CHAPTER VI

CONCLUSIONS AND FUTURE WORK

The previous chapter clearly illustrated that, while results were good for the homogeneous analyses, the implementation is not valid for interface modeling. Comparing the two approaches yields some important insights into possible explanations for the issues encountered.

The two codes used for the homogeneous and interface modeling differ in only three significant areas:

1. the presence or absence of interface enrichments
2. the equations used to characterize the near-tip stress fields
3. the size and layout of the stiffness matrix

If the first item were causing problems, the crack-mesh alignment study would show large disagreements between the alignment cases. That is because the interface implementation doesn't actually use interface enrichments when the crack is aligned with the interface, as explained in Section 3.4. Since all alignment cases are relatively in agreement, interface enrichment may be safely ruled out.

Any error in the implementation is most likely coming from the second and third areas. While the equations employed in the near-tip enrichment calculations have been verified to be correct, the values of the variables within those equations are calculated within a large block of code and some small bug could be fouling the analysis. The same is true for the construction of the stiffness matrix. The much larger number of dofs in the interface implementation means that its stiffness matrix

is more than six times as large as in the homogeneous case. Such an increase in complexity makes the tracing of a single keystroke error very difficult.

The explanation of a coding error is made more likely by the fact that the code asymptotically approaches an answer, albeit an incorrect one, with increasing mesh density. This stability is also confirmed by the linear nature of the solution, that is, the analysis is solved in one increment as expected. If the structure of the implementation were somehow fundamentally incorrect, the analysis would most likely either be forced to iterate to find a solution, or find no solution at all. Indeed, this is exactly what occurred during the early phases of development of the user element when key pieces of the code were found to be incorrectly implemented.

The next step for any future work should obviously be to correct the error in the interface implementation. Once that is completed, there are myriad directions the work could be taken, including extension into: three dimensions, large deformations, plasticity, and anisotropy. Challenges specific to the Abaqus implementation include developing methods to visualize the results (Abaqus/Viewer does not currently support the visualization of user elements), creating a preprocessing step to allow for the selective enrichment of nodes to reduce computational cost (as opposed to the current method of assigning all degrees of freedom to each node), and implementing quasi-static crack propagation through multiple steps definitions.

REFERENCES

[1] Anderson, A., *Fracture Mechanics: Fundamentals and Applications*. New York: CRC Press, 1995.

[2] Areias, "Analysis of three-dimensional crack initiation and propagation using the extended finite element method," *International Journal for Numerical Methods in Engineering*, vol. 63, pp. 760–788, 2005.

[3] Belytschko, "Elastic crack growth in finite elements with minimal remeshing," *International Journal for Numerical Methods in Engineering*, vol. 45, pp. 601–620, 1999.

[4] Belytschko, "Dynamic crack propagation based on loss of hyperbolicity with a new discontinuous enrichment," *International Journal for Numerical Methods in Engineering*, vol. 58, pp. 1873–1905, 2003.

[5] Chessa, "An extended finite element method for two-phase fluids," *Journal of Applied Mechanics*, vol. 70, pp. 10–17, 2003.

[6] Chopp, "Fatigue crack propagation of multiple coplanar cracks with the coupled extended finite element/fast marching method," *International Journal of Engineering Science*, vol. 41, pp. 845–869, 2003.

[7] Dolbow, "An extended finite element method for modeling crack growth with frictional contact," *Computational Methods in Applied Mechanics and Engineering*, vol. 19, pp. 6825–6846, 2001.

[8] Dolbow, "Coupling volume-of-fluid based interface reconstructions with the extended finite element method," *Computational Methods in Applied Mechanics and Engineering*, vol. 197, pp. 439–447, 2008.

[9] Duddu, "A combined extended finite element and level set method for biofilm growth," *International Journal for Numerical Methods in Engineering*, vol. 74, pp. 848–870, 2008.

[10] Elguedj, "Appropriate extended functions for x-fem simulation of plastic fracture mechanics," *Computational Methods in Applied Mechanics and Engineering*, vol. 195, pp. 501–515, 2006.

[11] Ewalds, *Fracture Mechanics*. New York: Edward Arnold, 1989.

[12] Gerstenberger, "An extended finite element method/lagrange multiplier based approach for fluid-structure interaction," *Computational Methods in Applied Mechanics and Engineering*, vol. 197, pp. 1699–1714, 2008.

[13] Gravouil, "Non-planar 3d crack growth by the extended finite element method and level sets. part ii: Level set update," *International Journal for Numerical Methods in Engineering*, vol. 53, pp. 2569–2586, 2002.

[14] Hettich, "Interface material failure modeled by the extended finite-element method and level sets," *Computational Methods in Applied Mechanics and Engineering*, vol. 195, pp. 4753–4767, 2006.

[15] Hettich, "Modeling of failure in composites by x-fem and level sets within a multiscale framework," *Computational Methods in Applied Mechanics and Engineering*, vol. 197, pp. 414–424, 2008.

[16] Huang, "Channel-cracking of thin films with the extended finite element method," *Engineering Fracture Mechanics*, vol. 70, pp. 2513–2526, 2003.

[17] Huang, "Inititation and arrest of an interfacial crack in a four-point bend test," *Engineering Fracture Mechanics*, vol. 72, pp. 2584–2601, 2005.

[18] Hughes, "Techniques for developing special finite element shape functions with particular references to signularities," *International Journal for Numerical Methods in Engineering*, vol. 15, pp. 733–751, 1980.

[19] Hutchinson, "Mixed mode cracking in layered materials," *Advances in Applied Mechanics*, vol. 29, pp. 63–191, 1992.

[20] Khoei, "Extended finite element method for three-dimensional large plasticity deformations on arbitrary interfaces," *Computational Methods in Applied Mechanics and Engineering*, vol. 197, pp. 1100–1114, 2008.

[21] Krongauz, "Efg approximation with discontinuous derivatives," *International Journal for Numerical Methods in Engineering*, vol. 41, pp. 1215–1233, 1998.

[22] Legrain, "Stress analysis around the crack tips in finite strain problems using the extended finite element method," *International Journal for Numerical Methods in Engineering*, vol. 63, pp. 290–314, 2005.

[23] Liang, "Evolving crack patterns in thin films with the extended finite element method," *Journal of Solids and Structures*, vol. 40, pp. 2343–2354, 2003.

[24] Matos, "A method for calculating stress intensities in bimaterial fracture," *International Journal of Fracture*, vol. 40, pp. 235–254, 1989.

[25] Melenk, "The partition of unity finite element method: Basic theory and applications," *Computer Methods in Applied Mechanics and Engineering*, vol. 139, pp. 289–314, 1996.

[26] Moes, "A finite element method for crack growth without remeshing," *International Journal for Numerical Methods in Engineering*, vol. 46, pp. 131–150, 1999.

[27] Moes, "Extended finite element method for cohesive crack growth," *Engineering Fracture Mechanics*, vol. 69, pp. 813–833, 2002.

[28] Moes, "A computational approach to handle complex microstructure geometry," *Computer Methods in Applied Mechanics and Engineering*, vol. 192, pp. 3163–3177, 2003.

[29] Rice, J., "Elastic fracture mechanics concepts for interfacial cracks," *Journal of Applied Mechanics*, vol. 55, pp. 98–103, 1988.

[30] Shih, "Elastic-plastic analysis of cracks on bimaterial interfaces: part-i small scale yielding," *Journal of Applied Mechanics*, vol. 55, pp. 299–316, 1988.

[31] Simone, "Partition of unity-based discontinuous elements for interface phenomena: Computational issues," *Communications in Numerical Methods in Engineering*, vol. 20, pp. 465–478, 2004.

[32] Simone, "A generalized finite element method for polycrystals with discontinuous grain boundaries," *International Journal for Numerical Methods in Engineering*, vol. 67, pp. 1122–1145, 2006.

[33] Smith, "The extended finite element method for boundary layer problems in biofilm growth," *Communications in Applied Mathematics and Computational Science*, vol. 2, pp. 35–56, 2007.

[34] Stolarska, "Modeling thermal fatigue cracking in integrated circuits by level sets and the extended finite element method," *International Journal of Engineering Science*, vol. 41, pp. 2381–2410, 2003.

[35] Sukumar, "Brittle fracture in polycrystalline microstructures with the extended finite element method," *International Journal for Numerical Methods in Engineering*, vol. 56, pp. 2015–2037, 2003.

[36] Sukumar, "Extended finite element method and fast marching method for three-dimensional fatigue crack propagation," *Engineering Fracture Mechanics*, vol. 70, pp. 29–48, 2003.

[37] Sukumar, "Partition of unity enrichment for bimaterial interface cracks," *International Journal for Numerical Methods in Engineering*, vol. 59, pp. 1075–1102, 2004.

[38] Suo, "Mechanics of interface fracture," tech. rep., Ph.D. Thesis, Division of Applied Sciences, Hardvard University, Cambridge, MA, USA, 1989.

[39] vanderSluis, "Advances in delamination modeling," *Nanopackaging: Nanotechnologies in Electronics Packaging*, vol. To appear, 2008.

[40] Wagner, "The extended finite element method for rigid particles in stokes flow," *International Journal for Numerical Methods in Engineering*, vol. 51, pp. 293–313, 2001.

[41] Williams, "The stress around a fault or crack in dissimilar media," *Bulletin of the Seismological Society of America*, vol. 49, no. 2, pp. 199–204, 1959.

[42] Zi, "New crack-tip elements for xfem and applications to cohesive cracks," *International Journal for Numerical Methods in Engineering*, vol. 57, pp. 2221–2240, 2003.

[43] Zilian, "The enriched space-time finite element method (est) for simultaneous solution of fluid-structure interaction," *International Journal for Numerical Methods in Engineering*, vol. 10, pp. 2258–2275, 2007.